Chemical Engineering Journal 502 (2024) 157721

Contents lists available at ScienceDirect

Chemical Engineering Journal

journal homepage: www.elsevier.com/locate/cej

Experimental and molecular simulation of carbon dioxide solubility in hexadecane at varying pressures and temperatures

Xiuyan Liu [a,b,c], Yahao Huang [a,*], Saeed Babaei [d], Bodhisatwa Hazra [e,f], Mehdi Ostadhassan [g,*]

[a] College of Resources and Environment, Yangtze University, Wuhan 430100, China
[b] Institute of Energy, Peking University, Beijing 100871, China
[c] Key Laboratory of Tectonics and Petroleum Resources Ministry of Education, China University of Geosciences, Wuhan, 430074, China
[d] Civil Engineering Faculty, K. N. Toosi University of Technology, Tehran Iran
[e] Academy of Scientific and Innovative Research, Ghaziabad 201002, (Uttar Pradesh), India
[f] CSIR-Central Institute of Mining and Fuel Research, Dhanbad 826001, (Jharkhand), India
[g] Institute of Geosciences, Christian-Albrechts-Universität, Kiel 24118, Germany

ARTICLE INFO

Keywords:
CO_2
Hexadecane
Raman spectroscopy
Enhanced oil recovery
Molecular simulation
Solubility
Swelling

ABSTRACT

CO_2-EOR can make underground storage efforts possible, addressing both energy demands and climate issues. This study establishes an in-situ method to measure the degree of CO_2 solubility in hexadecane in a wide range of P-T conditions. CO_2 and hexadecane with known volumes were mixed in silica capillaries and examined by Raman spectroscopy after reaching an equilibrium at certain P-T condition to establish a relationship between mole fraction of CO_2 in hexadecane and ratio of Raman peak area. Results showed that solubility of CO_2 decreases with increasing temperature and increases with pressure. Complementing the experimental data, hybrid grand canonical Monte Carlo/molecular dynamics (GCMC/MD) simulations were performed to study the swelling effect of CO_2/hexadecane system and the diffusion of CO_2 within hexadecane. Simulation results were validated against Raman spectroscopy and previously published CO_2 solubility data, as well as a genetic algorithm-based (GA) predictive model, all matching with high accuracy and conforming each other. Based on molecular simulation results, the necessity of accounting for volumetric changes in solubility calculations to enhance the accuracy of predictive models in similar systems was revealed. Additionally, in contrast to temperature, the effect of pressure on the diffusion coefficient remains relatively minimal. Ultimately, this study provides solutions for in-situ probing techniques to determine the solubility of various fluids in a wide range of P-T conditions, processes supporting CO_2-EOR and carbon storage operations underground.

1. Introduction

Energy security concerns every nation's future and development, especially in an era of global warming, climate, and environmental issues [1–3]. Replacing traditional fossil fuels with renewable energy is a global consensus to control the earth's surface temperature increase within 2 °C [4–6]. However, burning fossil fuels is still the main source of energy we need and will continue to be in the coming decades [7,8], while some scientists still believing there is an increasing demand for fossil fuels [9]. In this regard, unconventional resources such as shale oil and gas have addressed some of our needs where a decline in production from conventional resources in the past few decades has been prominent [10,11]. For instance, through exploiting shale reserves, the U.S. achieved its net energy export in 2019, with a remaining recoverable shale oil reserves of 3.25×10^{10} t and a current cumulative production of 3.17×10^{9} t [10,12]. Considering China, which is another country with major resources of unconventional shale plays, the total amount of shale oil and gas with high potential of production is estimated to be approximately $(150 - 300) \times 10^{8}$ t, of which those with good economic benefits are $(67 - 84) \times 10^{8}$ t [10]. On the other hand, power plants that operate based on fossil fuels generate one-third of the greenhouse gas emissions worldwide and are the primary focus of global carbon capture and storage (CCS) efforts [7].

To address both of these concerns that were explained above, carbon dioxide has been used as an injection material to rejuvenate shale oil reservoirs after primary production, which is called enhanced oil recovery (EOR) [13,14]. There are two types of gas injection methods, gas flooding and huff-n-puff [15]. While both have their own advantages

* Corresponding authors.
E-mail addresses: hyhtr08916@163.com (Y. Huang), mehdi.ostadhassan@ifg.uni-kiel.de (M. Ostadhassan).

https://doi.org/10.1016/j.cej.2024.157721
Received 29 July 2024; Received in revised form 5 November 2024; Accepted 14 November 2024
Available online 16 November 2024

and limitations [16]. For the well-to-well flooding process, the gas is continuously injected into the reservoir layers to displace the residual oil to adjacent production wells [16]. The huff-n-puff injection process is related to a single-well where the gas is cyclically injected into the reservoir [16]. Each cycle involves three phases: reservoir pressure build-up (huff), pressure equilibration and fluids interaction (soaking), and pressure depletion for production (puff) [16]. The injected CO_2, when dissolved in crude oil in shales, will reduce oil volume swelling and viscosity [17,18]. Moreover, supercritical CO_2 has been used to extract and separate a wide range of hydrocarbons from shale and coal under varying conditions [19]. Therefore, quantitatively measuring and predicting the solubility of CO_2 in oil systems would be important and essential for CCS and EOR operations [20–22].

Generally, the methods used for phase equilibrium studies include four types. (1) Analysis after gas and liquid with known compositions reach equilibrium at known P-T conditions, with the volumes of the mixture before and after equilibrium being measured to calculate the quantity of dissolved gas [23–30]. (2) Using a high-pressure optical cell filled with CO_2, with aqueous solvent added by a calibrated high-pressure pump until completely dissolved, then pressure is reduced until the first stable bubble appears [31]. (3) Injecting CO_2 into a liquid with known volume at certain P-T conditions and analyzing a small quantity of the liquid after reaching phase equilibrium to measure the solubility of CO_2 [32]. (4) Under known P-T conditions, a certain amount of gas is added to a container of known volume. The number of moles of gas can be calculated based on these conditions. The gas-containing vessel is then connected to another vessel with a known amount of solution. After equilibrium is reached, the system's temperature and pressure will stabilize and is recorded. The volume, temperature, and pressure changes of the remaining gas in the container allow for the calculation of the remaining gas amount. The difference between the initial and remaining gas amounts would be the quantity of gas dissolved in the solution. Finally, with the known solution amount, the gas solubility in the solution can be calculated. It should be noted that neither of these methods is considered in-situ measurement, which makes them time-consuming and not suitable when the pressure exceeds a certain threshold.

Raman spectroscopy is a technique that has been used increasingly for quantitative in-situ measurements of chemical components [33]. Due to its non-destructive manner, it has also been recently applied to the study of CO_2 solubility in various alkane solvents (hexane, octane, decane, and dodecane) using silica capillaries [34–36]. These studies demonstrated that the solubility of CO_2 in the alkanes decreased with increasing temperature and increased with increasing pressure [34], and adding hexane to decane at high pressure ($> \sim$6 MPa) can enhance CO_2 solubility [35]. In addition, the experiment revealed that the volume expansion factor of the CO_2 + dodecane increased with increasing pressure and decreased with increasing temperature [36]. However, experimental pressures have rarely exceeded 10 MPa, and there is a lack of integrated study of in-situ CO_2 solubility in alkane and molecular simulation on its subsequent impact on swelling and diffusion. It is better to test CO_2 solubility in longer chain length alkanes, which is known to better represent the chemical compositions of heavy oil. However, an alkane length exceeding 16 will cause strong fluorescence on Raman spectra. Thus, C_{16} (Hexadecane) is probably the best agent for Raman in-situ measurements of CO_2 solubility in alkanes. Moreover, it has been reported that hexadecane is similar to the average properties of Brazilian heavy oil [37]. Therefore, it is vital to implement experiments and in-situ Raman measurements of CO_2 solubility in hexadecane for realistic representation of real-world scenarios.

The quantitative measurements by Raman spectroscopy are made possible based on the fitted equations of the substance quantity and Raman parameters by measuring a series of standards. For solids, it is easy to prepare standards for Raman measurements as most solids are stable in air [38]. For fluids, the standards are commonly sealed in fused-silica capillary capsules available for Raman in-situ measurements and

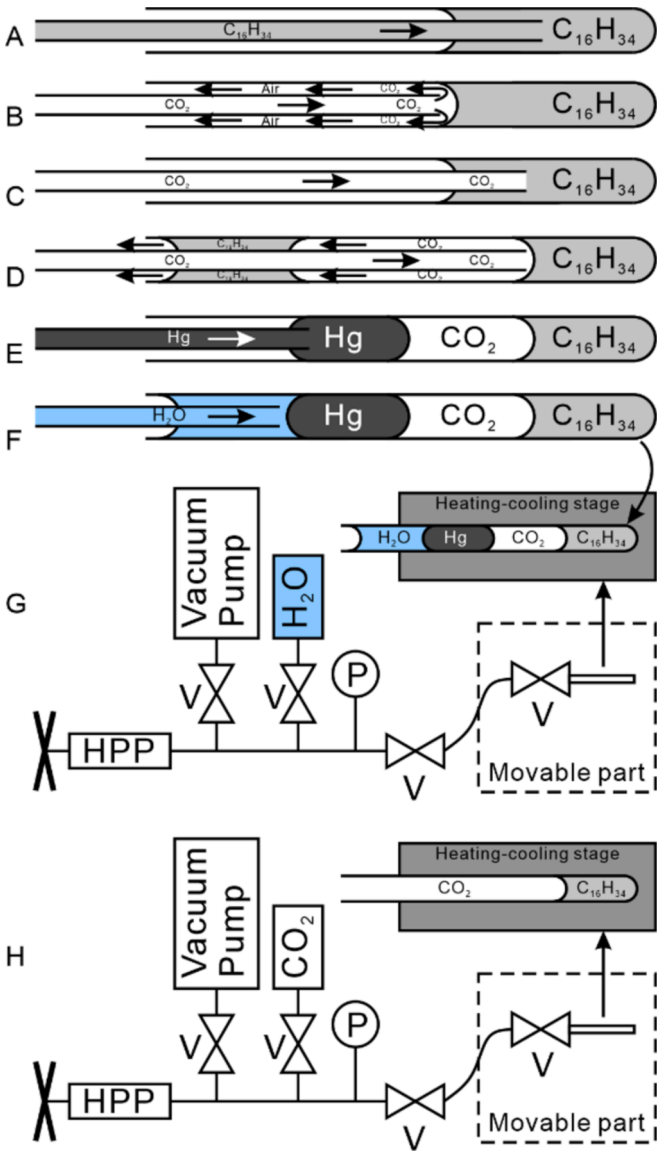

Fig. 1. Schematic diagram of the capillary and the pressurization device that is attached to it. P: pressure gauge; V: valve; HPP: high-pressure pump.

can also prevent the liquid inside from evaporation [39,40]. It has been noted that the intensity of the Raman signal is affected not only by the concentration of the substance under study but also by the internal signal processing of the Raman spectrometer, which could be affected by the wavelength of the excitation laser, the response of the CCD, the polarization response of the optics and grating, etc., Hence, every Raman spectrometer is expected to be calibrated by a series of standards before quantitative measurements [39].

In addition to experimental studies, molecular modeling has emerged as an increasingly valuable tool in petroleum related research, providing detailed insights into atomic and molecular interactions while facilitating the study of the structure, dynamics, and rheological properties of complex mixtures [41–44]. This approach is particularly advantageous as experimental studies are often costly, time-consuming, and limited in their ability to probe processes at the microscopic scale. For example, Kobayashi and Firoozabadi [45] employed Gibbs ensemble Monte Carlo (GEMC) simulations to investigate the relationship between the solubility of heavier alkanes in CO_2 and the effects of molecular structure and branching on solubility. Wang et al. [46] utilized molecular dynamics (MD) simulations to study the density and volumetric behavior of three typical n-alkanes (hexane, octane, and decane) across

various mole fractions of CO_2, examining conditions at temperatures ranging from 303 to 363 K and pressures up to 8.67 MPa. Similarly, Zhang et al. [47] explored CO_2 solubility in decane (C_{10}) and eicosane (C_{20}) over a pressure range of 5–30 MPa at a constant temperature of 311 K, providing further insights into solubility behavior under high-pressure conditions.

Thus, in this study, molecular simulations are accompanying experimental methods to overcome the limitations of experimental techniques to capture microscopic details. By integrating molecular modeling, we aim to gain a more comprehensive understanding of the molecular interactions and behaviors within the system, complementing experimental findings and providing valuable insights at both macroscopic and atomic scales. Furthermore, other objectives of this study is to establish a quantitative correlation between the degree of solubility of CO_2 in hexadecane ($C_{16}H_{34}$) and the ratio of their Raman peak areas in a wide range of pressures and temperatures in order to expand the database of CO_2 solubility in alkanes. We aim that the outcome of this study can support more successful CCS and EOR operations in shale oil reservoirs.

2. Methods

2.1. Capillaries

2.1.1. Hexadecanes with known CO_2 solubilities

Standards of hexadecanes with different CO_2 solubilities were prepared following: (1) hexadecane was injected into a silica capillary (inner diameter 0.3 mm and outer diameter 0.665 mm) from one end by using another thinner capillary (inner diameter 0.09 mm and outer diameter 0.2 mm) and centrifuged to the sealed end (Fig. 1A); (2) one end of the thinner capillary was connected to the valve of a CO_2 tank (99.99 %, Air Products) while the other end was put in water first to adjust the gas venting rate; (3) the open end of the thinner capillary was put close to the air-hexadecane surface in the capillary to remove the air in the capillary (Fig. 1B); (4) after around 3 to 5 min, the thinner capillary was quickly inserted into the sealed end of the thicker capillary (Fig. 1C), with the injected CO_2 pushing the hexadecane towards the open end of the capillary (Fig. 1D), then pulled out immediately when the injected CO_2 was enough; (5) the thinner capillary was then connected to a mercury at one end while the other end was put in the CO_2 in the capillary so that the mercury column of around 1 to 1.5 cm was injected for sealing (Fig. 1E); (6) Next a certain amount of water injected following the mercury column to suppress volatilization of the mercury (Fig. 1F). Finally, a valve was connected to the open water-filling end.

Note that in order to ensure the CO_2-hexadecane in the capillary is in a homogeneous state at the experimental P-T conditions, the length of the CO_2 and hexadecane columns in the capillary were estimated at room temperature to make sure the CO_2 would not reach its maximum solubility at experimental P-T conditions. The molality of CO_2 in hexadecane was calculated using equation (1):

$$m_{CO_2} = \frac{\rho_{CO_2}\pi r^2 L_{CO_2}/M_{CO_2}\sigma_{CO_2-C_{16}H_{34}}}{\rho_{C_{16}H_{34}}\pi r^2 L_{C_{16}H_{34}}/M_{C_{16}H_{34}} + \rho_{CO_2}\pi r^2 L_{CO_2}/M_{CO_2}\sigma_{CO_2-C_{16}H_{34}}} \quad (1)$$

where m_{CO_2} is the mole fraction of CO_2 in CO_2–$C_{16}H_{34}$ mixtures, r is the internal radii of the capillary, $M_{C_{16}H_{34}}$ and M_{CO_2} are molar masses of $C_{16}H_{34}$ and CO_2, which are 226 and 44, respectively, $\rho_{C_{16}H_{34}}$ and ρ_{CO_2} are the density of $C_{16}H_{34}$ and CO_2 at room temperature and pressure conditions, $L_{C_{16}H_{34}}$ and L_{CO_2} are the length of the $C_{16}H_{34}$ and CO_2 columns in the capillary at room temperature and pressure conditions, and $\sigma_{CO_2-C_{16}H_{34}}$ is Raman measuring bias coefficient between CO_2 and $C_{16}H_{34}$, which means the intensity of the Raman signal of CO_2 is $\sigma_{CO_2-C_{16}H_{34}}$ times higher than that of $C_{16}H_{34}$. In this study, the value of $\sigma_{CO_2-C_{16}H_{34}}$ is 1.8225.

2.1.2. Hexadecane saturated with CO_2

The capillary (inner diameter 0.3 mm, outer diameter 0.665 mm) was sealed at one end using a micro torch. The sealed end was then heated to suck around 0.5 cm $C_{16}H_{34}$ during the cooling phase. The capillary was then centrifuged to move the $C_{16}H_{34}$ to the sealed end and waited for the connection to the pressurization device.

2.2. Pressurization device and procedures

2.2.1. Known CO_2 solubility standards

Fig. 1G shows the schematic diagram of the experimental device that was prepared in this study. The prepared capillary was fixed on a heating and cooling stage as a movable part of the whole experimental device. The valve directly connected to the capillary was shut at the beginning, and the inner pressure of the capillary was at ambient pressure (1 atm). The capillary was then connected to the pressurization system, which was vacuumed and filled with water. Then, the valve that is directly connected to the capillary was opened; thereby, the high-pressure pump can add pressure to the capillary with a precision of 0.1 MPa, and the pressure can be read out on the pressure gauge. The capillary was then brought to the experimental pressure points (10, 20, 35, and 70 ± 0.2 MPa) and temperatures (25, 40, 60, 80, 100, 120, 140, 160, 180, and 200 ± 0.5 °C) and left for two or three days in order to ensure that the CO_2 and $C_{16}H_{34}$ mixture in the capillary would achieve thermal and pressure equilibrium. The mean thermal expansion coefficient of the capillary between 0 and 200 °C is 5.8×10^{-7}, which can be ignored [48].

2.2.2. Hexadecane saturated with CO_2

The prepared capillary was then put on the heating and cooling stage as a movable part connecting to the pressurization system (Fig. 1H). The valves, except the one that is adjacent to the CO_2 bottle were open to allow the vacuum pump to expel the air in the tubes. Then, the valve next to the CO_2 bottle was opened to let CO_2 wash the tubes. Then, the whole tube system was vacuumed again and filled with CO_2 (Fig. 1G). The experimental pressure (10, 20, 35, and 70 ± 0.2 MPa) was achieved by adjusting the high-pressure pump, while the temperatures (25, 40, 60, 80, 100, 120, 140, 160, 180, and 200 ± 0.5 °C) were controlled by a CAP 500 heating and cooling stage. Each P-T condition was sustained for at least 30 min to ensure the CO_2-$C_{16}H_{34}$ mixture within 20 μm from the interface, which was the target for Raman spectroscopy probing, reached phase equilibrium, which is recommended in the literature [49].

2.3. Raman spectroscopy

2.3.1. Raman spectrometer

The Ramna probe used in this study was a JY/Horiba LabRam HR spectrometer equipped with a 532 nm laser (Nd: YAG) with power of 5 mW, 50 × objective lenses (N.A. = 0.5), 1800 cm^{-1} grating, and a Peltier-cooled CCD (working at −70 °C). The confocal hole was 200 μm. The resolution of the measured spectra was 4 cm^{-1} at 1500 cm^{-1}. The peak position accuracy was ~ 0.02 cm^{-1} after peak fitting and Ne lamp calibration. The spectrometer was calibrated every morning using a silica wafer. Raman spectra were collected from 1200 to 1550 cm^{-1} with the acquisition time of 60 s × 4 accumulations for a single spectrum but it was increased according to the signal-to-noise ratio to acquire the intensity of the target Raman shift between 50,000 and 60,000 counts. The laser position was set on the hexadecane side of the capillary, near the CO_2-hexadecane interface (within 20 μm), where the liquid was easily saturated by CO_2 as previous experimental studies have suggested [49]. Each measurement was repeated three to fourteen times to ensure the stability and reproducibility of the obtained results, and the extracted data were reported as averaged values with standard deviations.

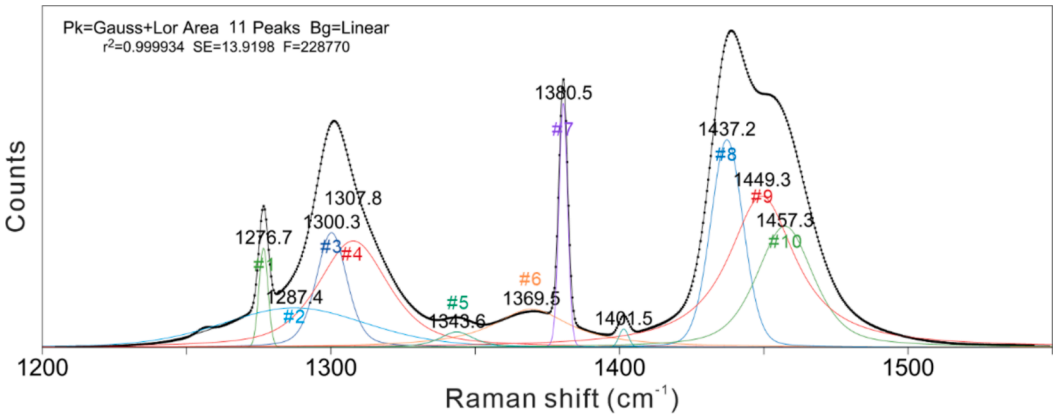

Fig. 2. Fitted Raman bands of CO_2 and $C_{16}H_{34}$ mixture in capillary at 35 MPa, 25 °C.

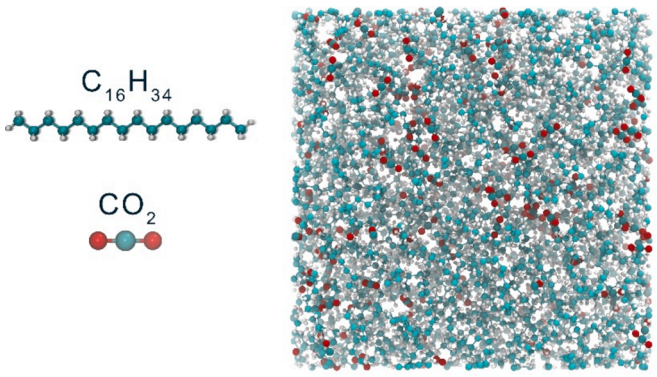

Fig. 3. Snapshot of the hexadecane/CO_2 system. Atom representation: cyan for carbon atoms, white for hydrogen atoms, red for oxygen atoms. (For interpretation of the references to colour in this figure legend, the reader is referred to the web version of this article.)

2.3.2. Raman data processing

The Raman peaks of CO_2 and $C_{16}H_{34}$ are imposed on a single Raman spectrum (Fig. 2). To accurately estimate the peak area ratio (PAR) of CO_2 and $C_{16}H_{34}$, the Raman bands (from 1200 to 1550 cm^{-1}) were fitted by using a Peakfit software. Thus, the PAR can be defined by the following formula:

$$PAR = \frac{A_{\#1} + A_{\#7}}{A_{\#2} + A_{\#3} + A_{\#4} + A_{\#5} + A_{\#6} + A_{\#8} + A_{\#9} + A_{\#10}} \quad (2)$$

2.4. Molecular simulations

In this study, we explored the solubility of CO_2 in hexadecane and its subsequent impact on the swelling behavior of hexadecane by employing grand canonical Monte Carlo (GCMC) simulations in the osmotic ensemble as well [50]. The snapshot of hexadecane/CO_2 is shown in Fig. 3. These simulations were conducted across a temperature range of 40, 100, 150, and 200 °C under pressures varying from 1 to 15 MPa. Initially, MD simulations using the NPT ensemble, comprising 162 octane molecules, were performed to equilibrate the system at designated pressures and temperatures.

Subsequently, a hybrid GCMC/NPT-MD simulation approach was utilized to determine CO_2 solubility. In the GCMC ensemble, the number of molecules of hexadecane is fixed, and the number of CO_2 is allowed to change according to its chemical potential imposed. For the GCMC simulations, consistent with our earlier research [51–53], we conducted additional simulations of pure gas in bulk conditions to establish the relationship between gas pressure and chemical potential. In Fig. S1. the density of bulk CO_2 was calculated as a function of temperature and pressure and compared with the National Institute of Standards and Technology (NIST) database [54]. This comparison was used to validate the accuracy of the force field parameters and chemical potential, as well as the reliability of the GCMC simulations. The results demonstrate that the employed computational model accurately captures the thermophysical properties of CO_2 across a range of conditions, confirming its applicability for further studies.

The hybrid simulation protocol incorporated 500 GCMC insertion/deletion trials for every 1000 NPT-MD steps. Given that CO_2 molecules were inserted with random positions and orientations and the system was subsequently relaxed using MD steps, no further Monte Carlo movements (i.e., translations and rotations) were performed [52,53,55]. The GCMC segments utilized the Metropolis algorithm [56] to ensure thermodynamic acceptance of molecular configurations can be obtained, whereas the MD segments implemented the velocity Verlet [57] integration scheme to solve Newton's equations of motion. An integration time step of 1 fs was maintained throughout the MD simulations. Temperature and pressure conditions were regulated using the Nosé–Hoover thermostat [58,59] and Nosé–Hoover barostat [60,61] with relaxation times of 0.1 and 1 ps, respectively.

For the molecular modeling, hexadecane was represented using the LOPLS force field [62], a refined version of the OPLS-AA [63] specifically optimized for long-chain hydrocarbons. CO_2 was modeled using the rigid EPM2 model [64] with a C-O bond length of 0.1149 nm and a linear O-C-O bond angle. The EPM2 force field parameters were derived from the vapor–liquid equilibrium (VLE) and critical properties of pure CO_2, ensuring high fidelity in simulation outcomes.

Intermolecular interactions were calculated using the geometric mean combining rules for Lennard-Jones (LJ) potentials and incorporated both the short-range LJ potential and Coulombic interactions up to a cutoff distance of 1.4 nm. Tail corrections were applied to account for LJ energies beyond this cutoff [65,66]. Long-range electrostatic interactions were computed via the particle–particle particle-mesh (PPPM) method, ensuring a computational precision of 10^{-4}. Periodic boundary conditions (PBC) were applied in all three directions. All simulations were executed using the LAMMPS software [67]. The final 5 ns of each 20 ns simulation were dedicated exclusively to data analysis, ensuring that equilibrium properties were robustly sampled and accurately reported.

After achieving equilibrium through GCMC/NPT-MD simulations, the system was further analyzed using MD simulations in the NVE ensemble for 10 ns to estimate gas diffusivity. The self-diffusivity of CO_2 was calculated using the Einstein relation, which involves the linear fit of mean-squared displacement (MSD) as a function of time [68,69].

$$D_s = \frac{1}{6N}\lim_{t\to\infty}\frac{d}{dt}\sum_{i=1}^{N} < |r_i(t) - r_i(0)|^2 > \quad (3)$$

Table 1
Calculated mole fraction of CO_2 in Hexadecane.

Sample ID	Temperature (°C)	Pressure (MPa)	Length of CO_2 column (mm)	Length of $C_{16}H_{34}$ column (mm)	Calculated mole fraction of CO_2
1	8.3	0.1	80.5	7.046	0.0732
2	15.1	0.1	144	4.36	0.1822
3	23.5	0.1	228	3.398	0.3054
4	16.3	0.1	224.2	1.36	0.5255
5	15.1	0.1	243	1.284	0.5651
6	13.8	0.1	225.5	0.386	0.7984

where N is the total number of inserted gas molecules, $\langle |r_i(t) - r_i(0)|^2 \rangle$ is the *MSD*, *r(t)* and *r(0)* are the positions of a molecule at time t and 0, respectively. Unwrapped trajectories were recorded every 2 ps, and only the first half of the simulation points were considered as time origins to ensure accurate calculations [70,71]. Diffusion coefficients were obtained using the diffusion coefficient analysis tool available in VMD [72].

2.5. Genetic algorithm-based model

A genetic algorithm-based (GA) model of the solubility of CO_2 in alkanes was proposed by Emera and Sarma [73] and was used to compare the results of CO_2 solubility in hexadecane in this study that was obtained in both simulation and experiments. The GA model is applied to predict the physical properties of CO_2-oil mixtures, as it takes into account both live and dead oil data with a thorough consideration of all major affecting parameters, achieving high accuracy [73].

In the GA model, the solubility of CO_2 is expressed by equation (4) as follows:

$$m_{CO_2} = 2.238 - 0.33y + 3.235y^{0.6474} - 4.8y^{0.25656} \quad (4)$$

where $y = v[0.006897 * \frac{(1.8T+32)^{0.8}}{P_s}]^{\exp(\frac{1}{MW})}$, v, the gravity of oil (density at 15.56°), MW, oil molecular weight, P_s, saturation pressure, MPa.

When the temperature is lower than the critical temperature of CO_2, and the pressure is higher than the liquifying pressure of CO_2, the solubility of CO_2 is more suitably expressed by equation (5):

$$m_{CO_2} = 0.033 + 1.44y - 0.7716y^2 + 0.2176y^3 - 0.02183y^4 \quad (5)$$

where $y = n(\frac{P_s}{P_{liq}})^{\exp(\frac{1.8T+32}{MW})}$, n, GA population size and number of components in the mixture, P_{liq}, CO_2 liquefaction pressure at the specified temperature, MPa.

3. Results

3.1. Mole fraction of CO_2 in capillary standards

Six capillary standards were prepared in the lab at room P-T conditions (Table 1). Herein, the m_{CO_2} was calculated using equation (1) which was found from 0.0732 to 0.7984.

3.2. Raman spectra at different P-T conditions

All the obtained Raman spectra of CO_2 and hexadecane show imposed Raman peaks as presented in Fig. 4. As the increase of mole fraction of CO_2 in hexadecane takes place, the total area of Raman peak area of CO_2 increases compared to that of hexadecane. Besides, Raman shifts (e.g., at 1275 and 1400 cm^{-1}) move towards higher wavenumbers as temperature and pressure increases. In addition, the shape of the Raman peaks gradually becomes wider and flatter as temperature increases from 25 to 200 °C (e.g., at 1300 and 1450 cm^{-1}).

3.3. Measured Raman PAR and best fit

A total of 123 averaged PAR values of the capillary standards were obtained at temperatures from 25 to 200 °C and pressures from 10 to 70 MPa, with the results (Supplementary Table S1) shown as PAR/m_{CO_2} vs. temperature cross-plots in Fig. 5.

It shows that at a fixed CO_2 solubility, the PAR/m_{CO_2} decreases as temperature increases. Likewise, decline in PAR/m_{CO_2} induced by elevated temperature is more significant in capillary samples with higher CO_2 solubilities. In contrast, the pressure seems to have a minor impact on the PAR/m_{CO_2} in most capillary samples (except sample No.2 with $m_{CO_2} = 0.1822$). Thus, the pressure was not considered a parameter in the best-fit polynomial as follows:

$$PAR/m_{CO_2} = C_1 + C_2T + C_3T^2 + C_4XT + C_5X + C_6X^2 + C_7X^3 (R^2 = 0.99) \quad (6)$$

where X is m_{CO_2} and T is temperature in °C. The coefficients are listed in

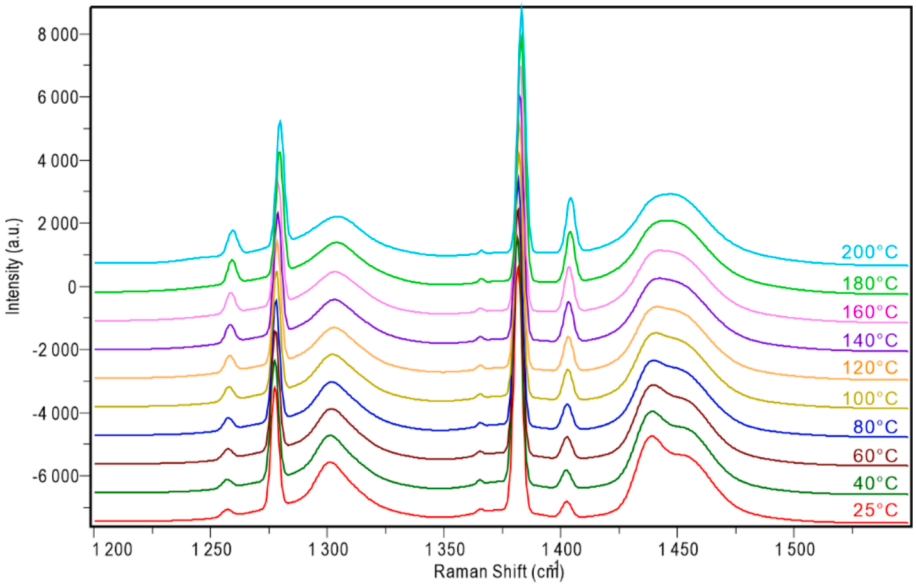

Fig. 4. Typical Raman spectra of standards. 25 – 200 °C, 35 MPa, $mCO_2 = 0.5255$.

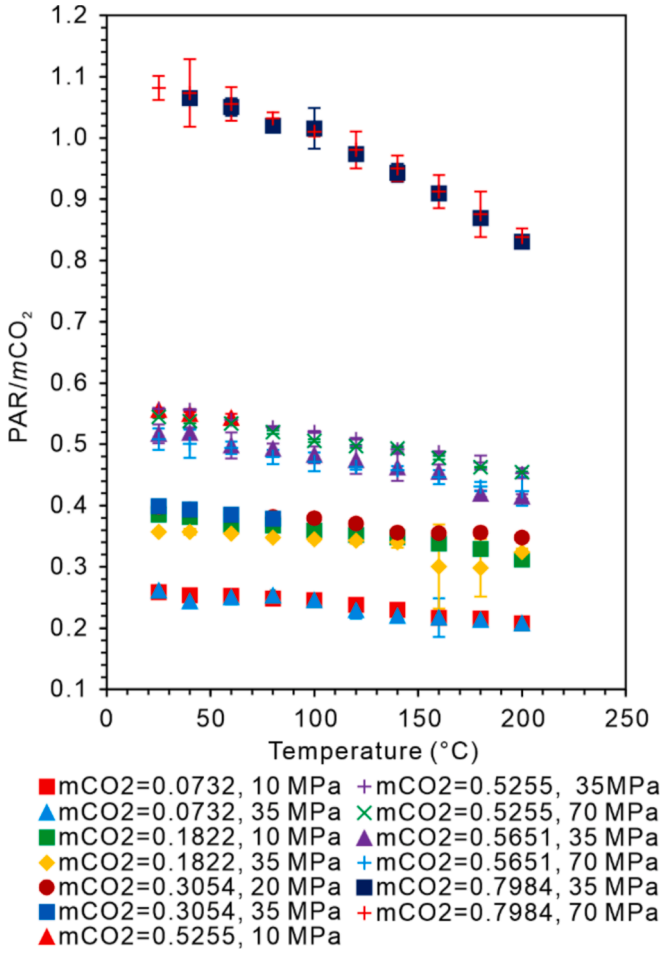

Fig. 5. Cross-plot of PAR/m_{CO_2} vs. temperature at different pressures and m_{CO_2}. Error bar: 1σ. Some error bars are within the size of the points.

Table 2
Coefficients of equation (6).

	Coefficients
C1	2.19E-01
C2	2.07E-04
C3	−6.70E-07
C4	−1.54E-03
C5	2.60E-01
C6	−3.89E-01
C7	1.76E + 00

Table 2.

3.4. Solubility of CO_2 in hexadecane

Based on equation (6) and PAR measured at the saturated state of CO_2 in hexadecane, its solubility was then calculated from 25 to 200 °C and 1 to 15 MPa. The results obtained in this study (solid squares and circles) as well as those calculated by the GA model (curves), are shown as temperature vs. m_{CO_2} cross-plot in Fig. 6., and listed in Table S2. It shows that the solubility of CO_2 in hexadecane decreases with increasing temperature while it increases with increasing pressure. At 1 MPa, the m_{CO_2} decreases by around 0.112 as temperature increases from 25 to 200 °C. However, the drop in solubility increases to around 0.371 at 15 MPa (Fig. 6). Furthermore, at 25 °C, increasing pressure from 1 to 15 MPa would cause the m_{CO_2} to rise by around 0.706, whereas at 200 °C, pressure increase from 1 to 15 MPa would cause the m_{CO_2} to rise by around 0.446 (Fig. 6).

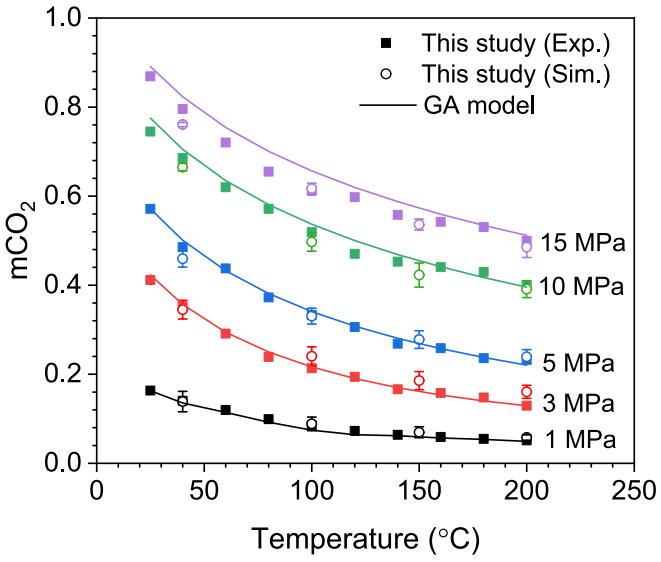

Fig. 6. Cross-plot of mCO_2 in this study and GA model.

4. Discussion

4.1. Error and uncertainty

The errors and uncertainties may originate from processing the Raman signal and P-T controlling devices. In this study, the temperature was controlled by a Linkam heating and cooling stage, with the temperature uncertainty within ± 0.5 °C. In addition, the fluctuation of pressure during the experiments was ± 0.2 MPa. According to the results presented in Fig. 5, the pressure variation has no significant impact on PAR/mCO_2 values; however, the effect of temperature is only significant when the temperature span is large. Therefore, the uncertainties of P-T conditions are considered negligible in this study. The Raman spectra were recorded 3 to 14 times at each P-T condition, and the averaged PAR/mCO_2 values were used for fitting and calculation, with a standard deviation of less than 7 % and an average standard deviation of less than 1 %. In Fig. 5, most error bars are within the size of the data points. Thus, the uncertainties in PAR/mCO_2 values are also considered insignificant in this study's fitted and calculated results, which makes us conclude that the results are valid.

4.2. Comparison with the molecular simulations and GA model

As shown in Fig. 6, the calculated m_{CO_2} from the PAR measured by Raman in this study closely aligns with those obtained from molecular simulations and the GA model. There exists a few exceptions (data points) at 15 MPa and 40 °C from molecular simulations, and two data points at 100 °C and 120 °C at 1 MPa, which deviate from the GA model by approximately 13 %. For the remaining data, discrepancies with the GA model are less than 8 %, with over 70 % of the data exhibiting deviations of less than 2 % (Table S2). Therefore, the data presented in this study are considered quite accurate. The solubility of CO_2 plays a pivotal role in influencing hydrocarbon viscosity and its consequent swelling, thereby enhancing mobility, relative permeability, and ultimately facilitating improved hydrocarbon recovery. Employing molecular modeling provides substantial insights into hydrocarbon recovery processes within reservoirs and aids in elucidating the mechanisms behind CO_2-induced hydrocarbon swelling.

While many molecular simulation studies often overlook the effects of swelling and flexibility [51,66,74], this research addresses these aspects by defining the swelling factor as the volume ratio of CO_2-

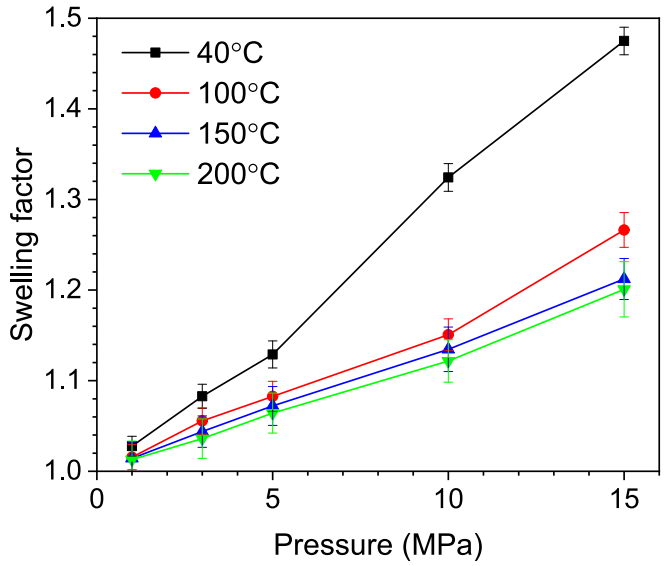

Fig. 7. Swelling factor as a function of pressure at various temperatures.

saturated hexadecane to that of pure hexadecane under identical conditions [46,50]. As depicted in Fig. 7, the swelling factor of hexadecane is positively correlated with pressure and inversely correlated with temperature, a consequence of the augmented solubility of CO_2 at elevated pressures and reduced temperatures. To further investigate the increase in swelling with increasing pressure, the pore size distribution (PSD) was calculated by Poreblazer v.4 software [75] for pressures of 1, 5, and 15 MPa at different temperatures, both before and after CO_2 solubility. As shown in Fig. 8, the PSD data support the observed swelling, indicating that the hexadecane microstructure changes more significantly with CO_2 solubility at higher pressures, leading to an increase in accessible space. The study reports swelling factors in the range of 1.01 and 1.47 at pressures from 1 to 15 MPa and temperatures between 40 °C and 200 °C (Fig. 7). In the temperature range of 150 to 200 °C, the temperature has minimal influence on the swelling factor, with pressure being the primary factor driving the swelling. However, as the temperature decreases, particularly at 40 °C, the swelling becomes more pronounced at a given pressure, with this effect becoming more substantial as pressure increases.

Moreover, when compared to octane [50], hexadecane demonstrates a reduced swelling factor. Octane, possessing a shorter carbon chain length (C_8H_{18}), exhibits greater molecular flexibility than hexadecane ($C_{16}H_{34}$). This flexibility allows octane molecules to more readily incorporate CO_2 molecules, resulting in a more significant volumetric expansion of the liquid phase.

Radial distribution functions (RDF) are crucial structural characteristics that provide insights into atomic packing [56]. In molecular simulations, RDFs can be obtained based on atomic coordinates. Fig. 9 presents the RDF of CO_2 with different atoms of hexadecane molecules at a pressure of 10 MPa at 100 °C and 200 °C. From Fig. 8a and 8b, we observe sharp peaks at short distances. The sharpest peak occurs between the carbon atom in CO_2 and the carbon atoms of hexadecane. The RDF analysis shows that the carbon atom of CO_2 interacts more strongly with the carbon atoms in the methyl groups (CH_3) than those in the methylene groups (CH_2) of hexadecane. This can be explained by the

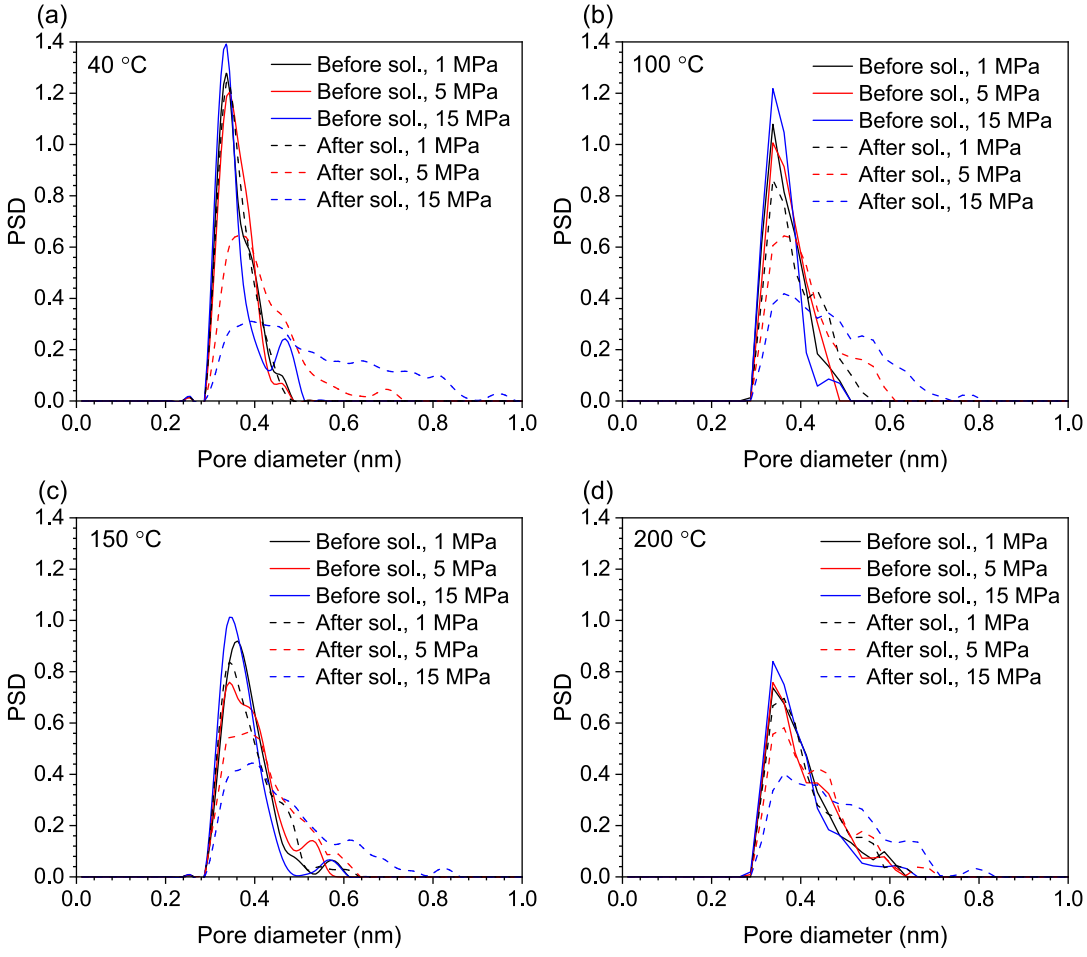

Fig. 8. Pore size distribution at 1, 5, and 15 MPa pressures at temperatures of (a) 40°C, (b) 100°C, (c) 150°C, and (d) 200°C.

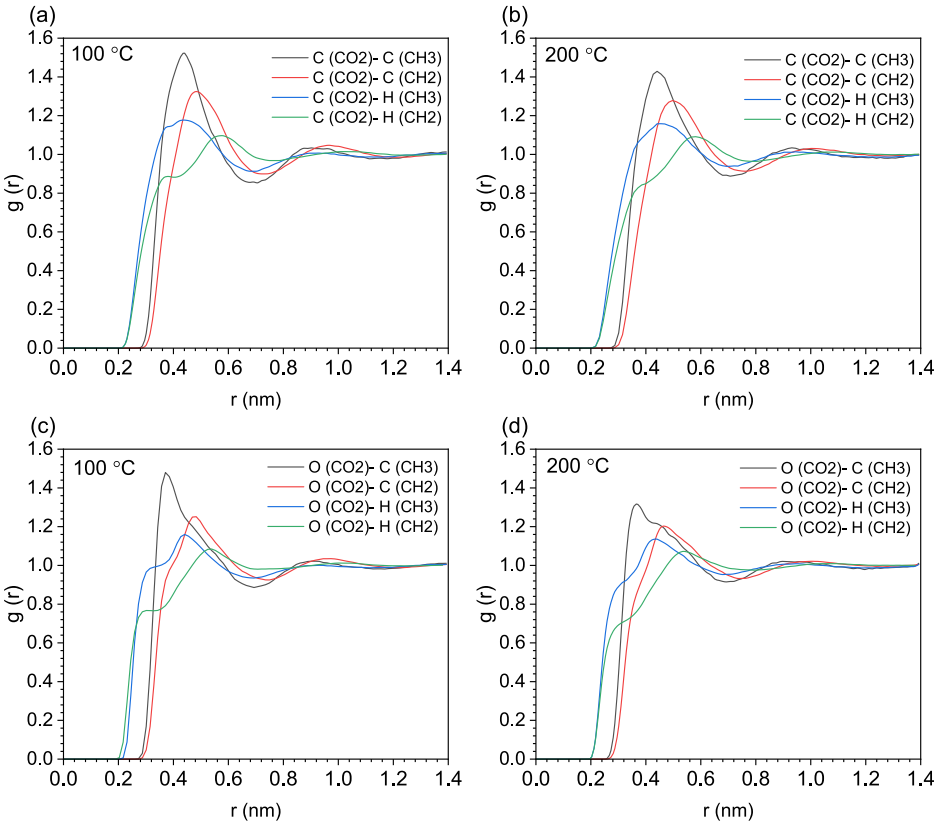

Fig. 9. Radial distribution function between the carbon atom of CO_2 and different atoms. of hexadecane at a pressure of 10 MPa at (a) 100 °C and (b) 200 °C, and between the oxygen atom of CO_2 and different atoms of hexadecane at (a) 100 °C and (b) 200 °C.

differences in their positions and electronic environments.

Methyl groups are located at the ends of the hexadecane molecule, making them more accessible for interactions with CO_2. They are less crowded and easier for CO_2 to reach than the methylene groups, which are buried within the alkane chain. This accessibility allows CO_2 to interact more readily with the carbon atoms in CH_3 groups. Additionally, the electron-donating nature of the methyl groups enhances their ability to interact with CO_2. The linear structure of hexadecane means that the methylene groups are less exposed, making them less available for interaction with CO_2.

Furthermore, we observed oxygen peaks at a shorter distance than carbon by comparing the RDF of carbon atoms in the methyl groups with carbon and oxygen atoms in CO_2. This specifies that linear CO_2 molecules adsorb perpendicular to the methyl groups.

4.3. Comparison with previous studies

Several studies have reported CO_2 solubility in hexadecane at certain P-T conditions. In Tanaka et al. [76] study, the m_{CO_2} at 40 °C and 3.103 MPa is 0.319, whereas the m_{CO_2} at 40 °C and 3 MPa in this study is 0.352, with a difference of 10.3 %. Breman et al. [77] reported the m_{CO_2} of 0.1417 at 201.15 °C and 2.97 MPa, while in this study, the measured value at 200 °C and 3 MPa is 0.1294, with the difference between −8.7 %. Sebastian et al. [78] reported the m_{CO_2} of 0.2575 at 189.9 °C and 5.01 MPa, whereas in this study at 5 MPa, the m_{CO_2} is 0.2360 at 180 °C and 0.2334 at 200 °C, respectively. Although the differences in temperature are around 10 °C, the variations of m_{CO_2} are less than 10 % (Table 3). Therefore, the CO_2 solubility measured in this study is considered acceptable, with a tolerance of around 10 % considering molecular simulation results verified the experimental outcome as well.

Table 3
Comparison of CO_2 solubility in this study and previous studies.

Temperature (°C)	Pressure (MPa)	mCO$_2$	Difference (%)	Reference
40	3.103	0.319		Tanaka et al. [76]
40	3	0.352	10.3	This study
201.15	2.97445	0.1417		Breman et al. [77]
200	3	0.1294	−8.7	This study
189.9	5.01	0.2575		Sebastian et al. [78]
180	5	0.2360	−8.4	This study
200	5	0.2334	−9.4	This study

4.4. Implications for CCS and EOR

CO_2-enhanced oil recovery is a major EOR method, except for thermal and chemical EOR [79]. The injected CO_2 mixes with oil, decreases oil's viscosity, and moves through fractures to the production well by expansion [22]. Oil production has shown an increase in light hydrocarbon components after CO_2-EOR, consistent with what was discussed above, which is that hexadecane has a smaller swelling factor than octane due to its longer chain length. However, this study implies that when performing CO_2-EOR, pressure is expected to increase while temperature is suppressed to achieve higher CO_2 solubility in hydrocarbons. Moreover, Fig. 7 implies that rather than temperature, pressure is much more important for increasing the swelling factor.

Also, the injection of CO_2 has been shown to significantly change the thermodynamic properties of crude oils, affecting their diffusion and migration. To improve these processes, it's crucial to understand how CO_2 diffuses in hexadecane under different temperature and pressure conditions. For instance, the MSD of CO_2 in hexadecane was computed

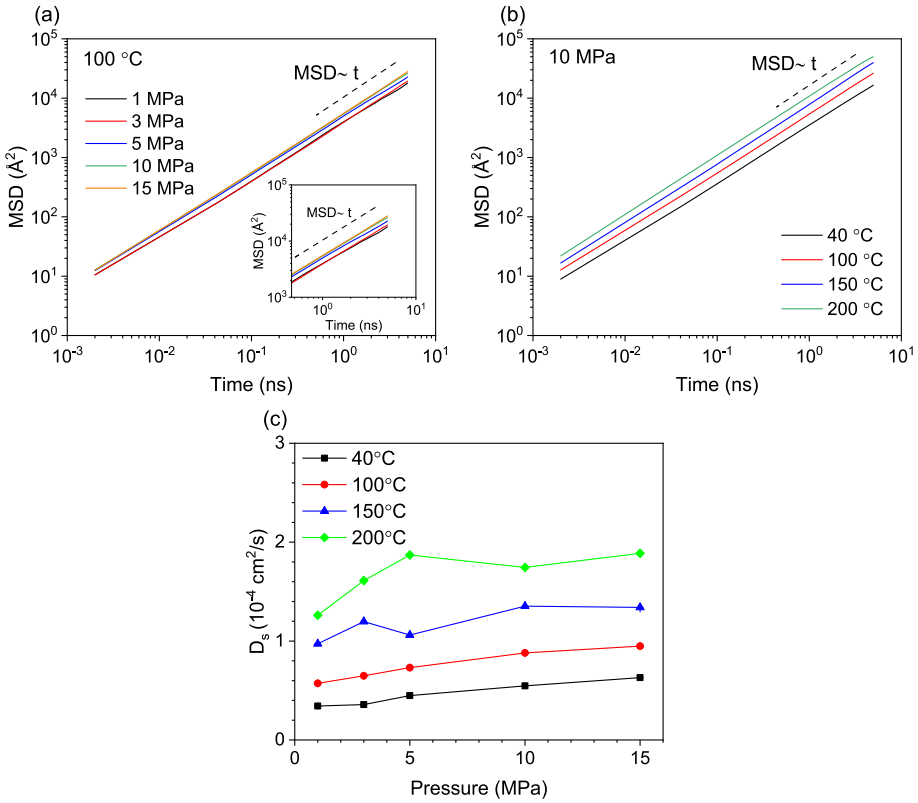

Fig. 10. MSD of CO_2 in a hexadecane/CO_2 system as a function of time in log–log scale at (a) 100 °C under various pressures, (b) 10 MPa across various temperatures, (c) self-diffusion coefficient of CO_2 in a hexadecane/CO_2 system as a function of pressure at various temperatures.

at 100 °C across a range of pressures and at 10 MPa over a range of temperatures, as shown in Fig. 10a and b. In the long-time regime, the molecular motion transitions to Brownian behavior, characterized by the linear scaling of the MSD with time (MSD ~ t) [80]. In this study, this transition to the Brownian motion regime occurs at approximately t = 1 ns. The increase in the slope of the MSD versus time interval curves with rising pressure and temperature signifies an enhancement in the mobility of CO_2 within the hexadecane matrix under these conditions. From the MSD data, we derived the self-diffusion coefficient and plotted its dependence on pressure across different temperatures in Fig. 10c. The findings indicate a clear dependence of the self-diffusion coefficient on both temperature and pressure. Specifically, Fig. 10c reveals that the CO_2 self-diffusion coefficients in hexadecane range from 10^{-4} to 10^{-5} cm^2/s depending on temperature and pressure, consistent with previously reported values [46,47].

Furthermore, the data reveal that the effect of temperature on CO_2 self-diffusion is more pronounced than pressure within the studied range. Beyond a pressure of 5 MPa, additional pressure increments do not significantly affect the self-diffusion coefficient, suggesting a saturation effect at higher pressures. This finding underscores the predominant influence of temperature in regulating the diffusion properties within the conditions explored in this study. In addition, a comparative analysis between decane (C_{10}) and eicosane (C_{20}) [47] reveals that the self-diffusion coefficient of CO_2 in hexadecane (C_{16}) falls between the values observed for the lighter and heavier alkanes. This trend indicates that CO_2 mobility decreases as the alkane's molecular weight increases. The reduction in CO_2 diffusivity with increasing alkane chain length is likely due to the enhanced molecular interactions and increased viscosity associated with longer carbon chains, which restrict the diffusion pathways of CO_2 molecules.

Ultimately, in this study we compared MS and experimental results with those obtained from a predictive model which showed a good agreement overall. As a result, considering thet fact that artificial intelligence (AI) or machine learning (ML) has increasingly gained popularity in dealing with CCS and EOR engineering problems [81–86], researchers should take advantage of generating large amount of data from simulation studies that have overlap in certain PT condition with the experiments and try to predict behavior of gas-hydrocarbon mixture systems. Finally, the results of this study and similar ones can be used to train AI or ML models to more accurately predict CO_2 behavior during the EOR of heavy oil reservoirs at various temperature and pressure conditions.

5. Conclusions

This study introduced an in-situ Raman spectroscopy method to quantify CO_2 solubility in hexadecane. Using standard capillary samples, we assessed the CO_2-saturated hexadecane across a temperature range of 25 to 200 °C and a pressure range of 1 to 15 MPa. Our findings indicate that the mole fraction of CO_2 in hexadecane decreases with increasing temperature and increases with increasing pressure. The results are comparable with molecular simulations, previously published CO_2 solubility data, and the GA model, denoting Raman spectroscopy is suitable for analyzing the behavior of the CO_2-hexadecane mixture, which subsequently can support a better understanding of CO_2-enhanced oil recovery. Furthermore, molecular simulations revealed swelling factors between 1.01 and 1.47 at pressures from 1 to 15 MPa and temperatures between 40 °C and 200 °C. Additionally, the study revealed that increased pressure and temperature would enhance the diffusion of CO_2 within alkane molecules; however, the impact of pressure on the diffusion process remains relatively limited. RDF results show that CO_2 interacts more strongly with the carbon atoms in the methyl groups (CH_3) than those in the methylene groups (CH_2) of hexadecane due to their greater accessibility for interactions with CO_2. These results underscore the necessity of accounting for volumetric changes in solubility calculations to enhance the accuracy of predictive

models in similar systems. Finally, experimental results accompanied by molecular modeling can be used in training AI and ML models to improve the accuracy of predicting CO_2 behavior in heavy oils underground at various temperature and pressure conditions.

CRediT authorship contribution statement

Xiuyan Liu: Conceptualization, Data curation, Formal analysis, Writing – original draft. **Yahao Huang:** Formal analysis, Validation, Data curation. **Saeed Babaei:** Conceptualization, Data curation, Formal analysis, Validation, Visualization, Writing – original draft. **Bodhisatwa Hazra:** Visualization, Validation, Data curation. **Mehdi Ostadhassan:** Writing – review & editing, Investigation, Resources, Supervision, Project administration, Methodology, Funding acquisition.

Declaration of competing interest

The authors declare that they have no known competing financial interests or personal relationships that could have appeared to influence the work reported in this paper.

Acknowledgement

This work was funded by the National Natural Science Foundations of China (No.42302154). Authors would like to extend their gratitude toward the editor who gave us the chance to revise the paper and submit an improved version. Most importantly we extend our thanks to respected reviewers who generously provided us with their comments and feedback which was necessary to improve technical quality of this manuscript.

Appendix A. Supplementary data

Supplementary data to this article can be found online at https://doi.org/10.1016/j.cej.2024.157721.

Data availability

data is uploaded in SI

References

[1] M. Asif, T. Muneer, Energy supply, its demand and security issues for developed and emerging economies, Renew. Sustain. Energy Rev. 11 (7) (2007) 1388–1413, https://doi.org/10.1016/j.rser.2005.12.004.
[2] B.K. Sovacool, M.A. Brown, Competing dimensions of energy security: an international perspective, Annu. Rev. Env. Resour. 35 (2010) 77–108, https://doi.org/10.1146/annurev-environ-042509-143035.
[3] A. Bauen, Future energy sources and systems—acting on climate change and energy security, J. Power Sources 157 (2) (2006) 893–901, https://doi.org/10.1016/j.jpowsour.2006.03.034.
[4] S. Bilgen, K. Kaygusuz, A. Sari, Renewable energy for a clean and sustainable future, Energy Source 26 (12) (2004) 1119–1129, https://doi.org/10.1080/00908310490441421.
[5] A. Kalair, N. Abas, M.S. Saleem, A.R. Kalair, N. Khan, Role of energy storage systems in energy transition from fossil fuels to renewables, Energy Storage 3 (1) (2021), https://doi.org/10.1002/est2.135.
[6] D. Gielen, F. Boshell, D. Saygin, M.D. Bazilian, N. Wagner, R. Gorini, The role of renewable energy in the global energy transformation, Energ. Strat. Rev. 24 (2019) 38–50, https://doi.org/10.1016/j.esr.2019.01.006.
[7] P.H. Stauffer, G.N. Keating, R.S. Middleton, H.S. Viswanathan, K.A. Berchtold, R. P. Singh, R.J. Pawar, A. Mancino, Greening coal: breakthroughs and challenges in carbon capture and storage, Environ. Sci. Tech. 45 (20) (2011) 8597–8604, https://doi.org/10.1021/es200510f.
[8] V.S. Arutyunov, G.V. Lisichkin, Energy resources of the 21st century: problems and forecasts. can renewable energy sources replace fossil fuels, Russ. Chem. Rev. 86 (8) (2017) 777, https://doi.org/10.1070/RCR4723.
[9] X. Liu, J. Fan, H. Jiang, J. Pironon, H. Chen, C. Li, X. Lu, X. Yu, M. Ostadhassan, Fluid history of lower Cambrian Longwangmiao formation in the Anyue gas field (Sichuan Basin, SW China), Geoenergy Sci. Eng. 231 (2023) 212308, https://doi.org/10.1016/j.geoen.2023.212308.
[10] L. Wang, Y. Zhang, R. Zou, R. Zou, L. Huang, Y. Liu, Z. Meng, Z. Wang, H. Lei, A systematic review of CO2 injection for enhanced oil recovery and carbon storage in shale reservoirs, Int. J. Hydrogen Energy 48 (95) (2023) 37134–37165, https://doi.org/10.1016/j.ijhydene.2023.06.099.
[11] H. Zhang, H.V. Thanh, M. Rahimi, W.J. Al-Mudhafar, S. Tangparitkul, T. Zhang, Z. Dai, U. Ashraf, Improving predictions of shale wettability using advanced machine learning techniques and nature-inspired methods: implications for carbon capture utilization and storage, Sci. Total Environ. 877 (2023) 162944, https://doi.org/10.1016/j.scitotenv.2023.162944.
[12] EIA, February 2022 Monthly Energy Review February, U.S. Energy Information Administration, Washington, 2022.
[13] B. Jia, J.-S. Tsau, R. Barati, A review of the current progress of CO2 injection EOR and carbon storage in shale oil reservoirs, Fuel 236 (2019) 404–427, https://doi.org/10.1016/j.fuel.2018.08.103.
[14] J.J. Sheng, Enhanced oil recovery in shale reservoirs by gas injection, J. Nat. Gas Sci. Eng. 22 (2015) 252–259, https://doi.org/10.1016/j.jngse.2014.12.002.
[15] H. Yu, H. Xu, W. Fu, X. Lu, Z. Chen, S. Qi, Y. Wang, W. Yang, J. Lu, Extraction of shale oil with supercritical CO2: effects of number of fractures and injection pressure, Fuel 285 (2021) 118977, https://doi.org/10.1016/j.fuel.2020.118977.
[16] Y. Yu, L. Li, J.J. Sheng, A comparative experimental study of gas injection in shale plugs by flooding and huff-n-puff processes, J. Nat. Gas Sci. Eng. 38 (2017) 195–202, https://doi.org/10.1016/j.jngse.2016.12.040.
[17] B. Liu, J. Shi, B. Sun, Y. Shen, J. Zhang, X. Chen, M. Wang, Molecular dynamics simulation on volume swelling of CO2–alkane system, Fuel 143 (2015) 194–201, https://doi.org/10.1016/j.fuel.2014.11.046.
[18] A. Rostami, M. Arabloo, A. Kamari, A.H. Mohammadi, Modeling of CO2 solubility in crude oil during carbon dioxide enhanced oil recovery using gene expression programming, Fuel 210 (2017) 768–782, https://doi.org/10.1016/j.fuel.2017.08.110.
[19] P.J. Jarboe, P.A. Candela, W. Zhu, A.J. Kaufman, Extraction of hydrocarbons from high-maturity marcellus shale using supercritical carbon dioxide, Energy Fuel 29 (12) (2015) 7897–7909, https://doi.org/10.1021/acs.energyfuels.5b02059.
[20] K.S. Lee, J. Cho, J.H. Lee, CO2 storage coupled with enhanced oil recovery, Springer, p. 2020. https://doi.org/10.1007/978-3-030-41901-1.
[21] N. Mosavat, A. Abedini, F. Torabi, Phase behaviour of CO2–brine and CO2–oil systems for CO2 storage and enhanced oil recovery: experimental studies, Energy Procedia 63 (2014) 5631–5645, https://doi.org/10.1016/j.egypro.2014.11.596.
[22] Z. Song, Y. Song, Y. Li, B. Bai, K. Song, J. Hou, A critical review of CO2 enhanced oil recovery in tight oil reservoirs of North America and China, Fuel 276 (2020) 118006, https://doi.org/10.1016/j.fuel.2020.118006.
[23] A.E. Markham, K.A. Kobe, The solubility of carbon dioxide and nitrous oxide in aqueous salt solutions, J. Am. Chem. Soc. 63 (2) (1941) 449–454, https://doi.org/10.1021/ja01847a027.
[24] S.Y. Yeh, R.E. Peterson, Solubility of carbon dioxide, krypton, and xenon in aqueous solution, J. Pharm. Sci. 53 (7) (1964) 822–824, https://doi.org/10.1002/jps.2600530728.
[25] K. Onda, E. Sada, T. Kobayashi, S. Kito, K. Ito, Salting-out parameters of gas solubility in aqueous salt solutions, J. Chem. Eng. Jpn. 3 (1) (1970) 18–24, https://doi.org/10.1252/jcej.3.18.
[26] A. Yasunishi, F. Yoshida, Solubility of carbon dioxide in aqueous electrolyte solutions, J. Chem. Eng. Data 24 (1) (1979) 11–14, https://doi.org/10.1021/je60080a007.
[27] G. Vázquez, F. Chenlo, G. Pereira, CO2 diffusivity in NaCl and CuSO4 aqueous-solutions, Afinidad 51 (453) (1994) 369–374.
[28] G. Vázquez, F. Chenlo, G. Pereira, J. Peaguda, Carbon dioxide solubility in aqueous solutions of sodium chloride, copper (ii) sulfate, potassium iodide and sodium bromide, An. Quim. (1994) 324–328.
[29] D.-Q. Zheng, T.-M. Guo, H. Knapp, Experimental and modeling studies on the solubility of CO2, CHC1F2, CHF3, C2H2F4 and C2H4F2 in water and aqueous NaCl solutions under low pressures, Fluid Phase Equilib 129 (1–2) (1997) 197–209, https://doi.org/10.1016/S0378-3812(96)03177-9.
[30] H. Teng, A. Yamasaki, Solubility of liquid CO2 in synthetic sea water at temperatures from 278 K to 293 K and pressures from 6.44 MPa to 29.49 MPa, and densities of the corresponding aqueous solutions, J. Chem. Eng. Data 43 (1) (1998) 2–5, https://doi.org/10.1021/je9700737.
[31] B. Rumpf, H. Nicolaisen, C. Öcal, G. Maurer, Solubility of carbon dioxide in aqueous solutions of sodium chloride: experimental results and correlation, J. Solution Chem. 23 (1994) 431–448, https://doi.org/10.1007/BF00973113.
[32] N. Zhu, Y. Song, Y. Zhang, W. Liu, F. Chang, Progress in measurement and model on solubility of CO2 under geological sequestration conditions, Environmental Science & Technology (china) 34 (3) (2011) 162–166.
[33] R.S. Das, Y. Agrawal, Raman spectroscopy: recent advancements, techniques and applications, Vib. Spectrosc 57 (2) (2011) 163–176, https://doi.org/10.1016/j.vibspec.2011.08.003.
[34] J.-L. Wang, Z.-H. Song, L.-J. Li, L.-L. Yang, Q.-Y. Wang, I.-M. Chou, Z.-Y. Pan, Integration of a fused silica capillary and in-situ Raman spectroscopy for investigating CO2 solubility in n-dodecane at near-critical and supercritical conditions of CO2, Pet, Sci 19 (6) (2022) 3124–3133, https://doi.org/10.1016/j.petsci.2022.06.014.
[35] J. Wang, Z. Zhang, Q. Wang, T. Lou, Z. Pan, M. Hu, Integrated a fused silica capillary cell and in situ Raman spectroscopy for determining the solubility of CO2 in n-decane and n-decane+ n-hexane system, Processes 11 (4) (2023) 1137, https://doi.org/10.3390/pr11041137.
[36] J. Wang, S. Zhou, K. Bei, I.-M. Chou, C. Lin, Z. Pan, A new approach for the measurement of the volume expansion of a CO2+ n-dodecane mixture in a fused silica capillary cell by Raman spectroscopy, Fuel 203 (2017) 113–119, https://doi.org/10.1016/j.fuel.2017.04.094.

[37] C. Campos, J.R. Penello, F.L.P. Pessoa, A.M.C. Uller, Experimental measurement and thermodynamic modeling for the solubility of methane in water and hexadecane, J. Chem. Eng. Data 55 (7) (2010) 2576–2580, https://doi.org/10.1021/je9007958.
[38] Q. Zhou, X. Xiao, L. Pan, H. Tian, The relationship between micro-Raman spectral parameters and reflectance of solid bitumen, Int. J. Coal Geol. 121 (2014) 19–25, https://doi.org/10.1016/j.coal.2013.10.013.
[39] M.-C. Caumon, J. Dubessy, P. Robert, A. Tarantola, Fused-silica capillary capsules (FSCCs) as reference synthetic aqueous fluid inclusions to determine chlorinity by Raman spectroscopy, Eur. J. Mineral. 25 (5) (2013) 755–763, https://doi.org/10.1127/0935-1221/2013/0025-2280.
[40] M.-C. Caumon, P. Robert, E. Laverret, A. Tarantola, A. Randi, J. Pironon, J. Dubessy, J.-P. Girard, Determination of methane content in NaCl–H_2O fluid inclusions by Raman spectroscopy. Calibration and application to the external part of the Central Alps (Switzerland), Chem. Geol. 378 (2014) 52–61, https://doi.org/10.1016/j.chemgeo.2014.03.016.
[41] R.M. Venable, A. Krämer, R.W. Pastor, Molecular dynamics simulations of membrane permeability, Chem. Rev. 119 (9) (2019) 5954–5997, https://doi.org/10.1021/acs.chemrev.8b00486.
[42] P. Morgado, J. Barras, P. Duarte, E.J.M. Filipe, Solubility of water in n-alkanes: new experimental measurements and molecular dynamics simulations, Fluid Phase Equilib 503 (2020) 112322, https://doi.org/10.1016/j.fluid.2019.112322.
[43] A. Obliger, C. Bousige, B. Coasne, J.-M. Leyssale, Development of atomistic kerogen models and their applications for gas adsorption and diffusion: a mini-review, Energy Fuel 37 (3) (2023) 1678–1698, https://doi.org/10.1021/acs.energyfuels.2c03633.
[44] W. Shi, R.L. Thompson, M.K. Macala, K. Resnik, J.A. Steckel, N.S. Siefert, D. P. Hopkinson, Molecular simulations of CO2 and H2 solubility, CO2 diffusivity, and solvent viscosity at 298 K for 27 commercially available physical solvents, J. Chem. Eng. Data 64 (9) (2019) 3682–3692, https://doi.org/10.1021/acs.jced.8b01228.
[45] K. Kobayashi, A. Firoozabadi, Effect of branching on mutual solubility of alkane–CO2 systems by molecular simulations, J. Phys. Chem. B 126 (41) (2022) 8300–8308, https://doi.org/10.1021/acs.jpcb.2c05774.
[46] Y. Wang, Y. Chen, J. Wang, Z. Pan, J. Liu, Molecular simulation study on the density behavior of n-alkane/CO2 systems, ACS Omega 6 (44) (2021) 29618–29628, https://doi.org/10.1021/acsomega.1c03889.
[47] J. Zhang, M. Seyyedi, M.B. Clennell, Molecular dynamics simulation of transport and structural properties of CO2–alkanes, Energy Fuel 35 (8) (2021) 6700–6710, https://doi.org/10.1021/acs.energyfuels.0c03788.
[48] W. Wang, M.-C. Caumon, A. Tarantola, J. Pironon, W. Lu, Y. Huang, Raman spectroscopic densimeter for pure CO2 and CO2-H2O-NaCl fluid systems over a wide PT range up to 360° C and 50 MPa, Chem. Geol. 528 (2019) 119281, https://doi.org/10.1016/j.chemgeo.2019.119281.
[49] W. Lu, H. Guo, I.-M. Chou, R. Burruss, L. Li, Determination of diffusion coefficients of carbon dioxide in water between 268 and 473 K in a high-pressure capillary optical cell with in situ Raman spectroscopic measurements, Geochim. Cosmochim. Acta 115 (2013) 183–204, https://doi.org/10.1016/j.gca.2013.04.010.
[50] J. Zhang, Z. Pan, K. Liu, N. Burke, Molecular simulation of CO2 solubility and its effect on octane swelling, Energy Fuel 27 (5) (2013) 2741–2747, https://doi.org/10.1021/ef400283n.
[51] S. Babaei, H. Ghasemzadeh, S. Tesson, Methane adsorption of nanocomposite shale in the presence of water: Insights from molecular simulations, Chem. Eng. J. 475 (2023) 146196, https://doi.org/10.1016/j.cej.2023.146196.
[52] B. Liu, S. Babaei, L. Bai, S. Tian, H. Ghasemzadeh, M. Rashidi, M. Ostadhassan, A dilemma in calculating ethane absolute adsorption in shale gas reservoirs: a theoretical approach, Chem. Eng. J. 450 (2022) 138242, https://doi.org/10.1016/j.cej.2022.138242.
[53] B. Liu, S. Babaei, M. Kanduč, S. Tian, L. Bai, Y. Xu, M. Ostadhassan, Helium expansion revisited: effects of accessible volume on excess adsorption in kerogen matrices, Chem. Eng. J. 493 (2024) 152690, https://doi.org/10.1016/j.cej.2024.152690.
[54] P. Linstorm, NIST chemistry webbook, NIST standard reference database number 69, J. Phys. Chem. Ref. Data, Monogr. 9 (1998) 1–1951.
[55] H. Ghasemzadeh, S. Babaei, S. Tesson, J. Azamat, M. Ostadhassan, From excess to absolute adsorption isotherm: the effect of the adsorbed density, Chem. Eng. J. 425 (2021) 131495, https://doi.org/10.1016/j.cej.2021.131495.
[56] D. Frenkel, B. Smit. Understanding molecular simulation: from algorithms to applications, Third ed., Elsevier, 2023 https://doi.org/10.1016/C2009-0-63921-0.
[57] L. Verlet, Computer "Experiments" on classical fluids. I. Thermodynamical properties of lennard-jones molecules, Physical Review 159(1) (1967) 98-103. https://doi.org/10.1103/PhysRev.159.98.
[58] S. Nosé, A unified formulation of the constant temperature molecular dynamics methods, J. Chem. Phys. 81 (1) (1984) 511–519, https://doi.org/10.1063/1.447334.
[59] S. Nosé, A molecular dynamics method for simulations in the canonical ensemble, Mol. Phys. 52 (2) (1984) 255–268, https://doi.org/10.1080/00268978400101201.
[60] S. Nosé, M.L. Klein, A study of solid and liquid carbon tetrafluoride using the constant pressure molecular dynamics technique, J. Chem. Phys. 78 (11) (1983) 6928–6939, https://doi.org/10.1063/1.444641.
[61] W.G. Hoover, Constant-pressure equations of motion, Phys. Rev. A 34 (3) (1986) 2499–2500, https://doi.org/10.1103/PhysRevA.34.2499.
[62] S.W.I. Siu, K. Pluhackova, R.A. Böckmann, Optimization of the OPLS-AA force field for long hydrocarbons, J. Chem. Theory Comput. 8 (4) (2012) 1459–1470, https://doi.org/10.1021/ct200908r.
[63] W.L. Jorgensen, D.S. Maxwell, J. Tirado-Rives, Development and testing of the OPLS all-atom force field on conformational energetics and properties of organic liquids, J. Am. Chem. Soc. 118 (45) (1996) 11225–11236, https://doi.org/10.1021/ja9621760.
[64] J.G. Harris, K.H. Yung, Carbon dioxide's liquid-vapor coexistence curve and critical properties as predicted by a simple molecular model, J. Phys. Chem. 99 (31) (1995) 12021–12024, https://doi.org/10.1021/j100031a034.
[65] K.M. Jablonka, D. Ongari, B. Smit, Applicability of tail corrections in the molecular simulations of porous materials, J. Chem. Theory Comput. 15 (10) (2019) 5635–5641, https://doi.org/10.1021/acs.jctc.9b00586.
[66] N. Sanchouli, S. Babaei, M. Kanduč, F. Molaei, M. Ostadhassan, Wetting behavior of kerogen surfaces: insights from molecular dynamics, Langmuir 40 (11) (2024) 5715–5724, https://doi.org/10.1021/acs.langmuir.3c03367.
[67] A.P. Thompson, H.M. Aktulga, R. Berger, D.S. Bolintineanu, W.M. Brown, P. S. Crozier, P.J. in 't Veld, A. Kohlmeyer, S.G. Moore, T.D. Nguyen, R. Shan, M. J. Stevens, J. Tranchida, C. Trott, S.J. Plimpton, LAMMPS - a flexible simulation tool for particle-based materials modeling at the atomic, meso, and continuum scales, Computer Physics Communications 271 (2022) 108171, https://doi.org/10.1016/j.cpc.2021.108171.
[68] E.J. Maginn, R.A. Messerly, D.J. Carlson, D.R. Roe, J.R. Elliot, Best practices for computing transport properties 1. Self-diffusivity and viscosity from equilibrium molecular dynamics [Article v1.0], Living Journal of Computational Molecular Science 1 (1) (2018) 6324, https://doi.org/10.33011/livecoms.1.1.6324.
[69] W. Kellouai, P. Judeinstein, M. Plazanet, J.-M. Zanotti, Q. Berrod, M. Drobek, A. Julbe, B. Coasne, Free volume theory of self-diffusion in zeolites: molecular simulation and experiment, Microporous Mesoporous Mater 381 (2025) 113305, https://doi.org/10.1016/j.micromeso.2024.113305.
[70] F. Perez, D. Devegowda, Hydrocarbon Self-diffusion and assessing the validity of Graham's Law under nanoporous confinement in shales, Energy Fuel 35 (13) (2021) 10512–10518, https://doi.org/10.1021/acs.energyfuels.1c00735.
[71] D. Keffer, The working man's guide to obtaining self diffusion coefficients from molecular dynamics simulations, Department of Chemical Engineering, University of Tennessee, Knoxville, USA (2001).
[72] T. Giorgino, Computing diffusion coefficients in macromolecular simulations: the Diffusion Coefficient Tool for VMD, Journal of Open Source Software 4 (41) (2019) 1698, https://doi.org/10.21105/joss.01698.
[73] M. Emera, H. Sarma, A genetic algorithm-based model to predict co-oil physical properties for dead and live oil, J. Can. Pet. Technol. 47 (02) (2008), https://doi.org/10.2118/08-02-52.
[74] M. Chen, B. Coasne, R. Guyer, D. Derome, J. Carmeliet, Role of hydrogen bonding in hysteresis observed in sorption-induced swelling of soft nanoporous polymers, Nat. Commun. 9 (1) (2018) 3507, https://doi.org/10.1038/s41467-018-05897-9.
[75] L. Sarkisov, R. Bueno-Perez, M. Sutharson, D. Fairen-Jimenez, Materials Informatics with PoreBlazer v4.0 and the CSD MOF Database, Chem. Mater. 32 (23) (2020) 9849–9867, https://doi.org/10.1021/acs.chemmater.0c03575.
[76] H. Tanaka, Y. Yamaki, M. Kato, Solubility of carbon dioxide in pentadecane, hexadecane, and pentadecane+ hexadecane, J. Chem. Eng. Data 38 (3) (1993) 386–388, https://doi.org/10.1021/je00011a013.
[77] B. Breman, A. Beenackers, E. Rietjens, R. Stege, Gas-liquid solubilities of carbon monoxide, carbon dioxide, hydrogen, water, 1-alcohols (1. ltoreq. n. ltoreq. 6), and n-paraffins (2. ltoreq. n. ltoreq. 6) in hexadecane, octacosane, 1-hexadecanol, phenanthrene, and tetraethylene glycol at pressures up to 5.5 MPa and temperatures from 293 to 553 K, J. Chem. Eng. Data 39 (4) (1994) 647–666, https://doi.org/10.1021/je00016a004.
[78] H.M. Sebastian, J.J. Simnick, H.-M. Lin, K.-C. Chao, Vapor-liquid equilibrium in binary mixtures of carbon dioxide+ n-decane and carbon dioxide+ n-hexadecane, J. Chem. Eng. Data 25 (2) (1980) 138–140, https://doi.org/10.1021/je60085a012.
[79] E.M. Mokheimer, M. Hamdy, Z. Abubakar, M.R. Shakeel, M.A. Habib, M. Mahmoud, A comprehensive review of thermal enhanced oil recovery: techniques evaluation, J. Energy Res. Technol. 141 (3) (2019) 030801, https://doi.org/10.1115/1.4041096.
[80] M. Kanduč, W.K. Kim, R. Roa, J. Dzubiella, Selective molecular transport in thermoresponsive polymer membranes: role of nanoscale hydration and fluctuations, Macromolecules 51 (13) (2018) 4853–4864, https://doi.org/10.1021/acs.macromol.8b00735.
[81] M. Mahdaviara, M.N. Amar, A. Hemmati-Sarapardeh, Z. Dai, C. Zhang, T. Xiao, X. Zhang, Toward smart schemes for modeling CO2 solubility in crude oil: application to carbon dioxide enhanced oil recovery, Fuel 285 (2021) 119147, https://doi.org/10.1016/j.fuel.2020.119147.
[82] M. Ali, Z. Hamdi, H. Elochukwu, S. Musa, M. Bataee, S. Behjat, Acceleration of CO2 Solubility Trapping Mechanism for Enhanced Storage Capacity Utilizing Artificial Intelligence, SPE Norway Subsurface Conference?, SPE (2024), https://doi.org/10.2118/218478-MS.
[83] A. Hassan, S. Elkatatny, A. Abdulraheem, Intelligent prediction of minimum miscibility pressure (MMP) during CO2 flooding using artificial intelligence techniques, Sustainability 11 (24) (2019) 7020, https://doi.org/10.3390/su11247020.
[84] N.A. Menad, A. Hemmati-Sarapardeh, A. Varamesh, S. Shamshirband, Predicting solubility of CO2 in brine by advanced machine learning systems: application to

carbon capture and sequestration, J. CO2 Util. 33 (2019) 83–95, https://doi.org/10.1016/j.jcou.2019.05.009.
[85] Y. Yang, B. Ju, G. Lü, Y. Huang, Machine learning methods for predicting CO2 solubility in hydrocarbons, Pet, Sci 21 (5) (2024) 3340–3349, https://doi.org/10.1016/j.petsci.2024.04.018.
[86] M.G. Rezk, A.F. Ibrahim, A.R. Adebayo, Uncertainty quantification for CO2 storage during intermittent CO2-EOR in oil reservoirs, Int. J. Coal Geol. 266 (2023) 104177, https://doi.org/10.1016/j.coal.2022.104177.